Electronic Supplementary Material (ESI) for RSC Sustainability.

Supplementary Information

Towards Sustainable TiO_2 Photoelectrodes Based on Cellulose Nanocrystals as a Processing Adjuvant

C. Martínez-Barón[1], V. Calvo[1], J. Hernández-Ferrer[1], B. Villacampa[2], A. Ansón-Casaos[1], J. M. González-Domínguez[1]*, W. K. Maser[1], A. M. Benito[1]

[1]Instituto de Carboquímica, ICB-CSIC, Miguel Luesma Castán 4, 50018 Zaragoza, Spain
[2]Departamento de Física de la Materia Condensada, INMA-CSIC, Universidad de Zaragoza, 50009, Zaragoza, Spain

*Corresponding author E-mail: jmgonzalez@icb.csic.es

Table of contents

TEM, size distribution and elemental analysis of CNC

TEM images of the type II CNC are presented in **Figure S1** and the distribution of diameters and heights of the CNC are in **Figure S2**. It can be observed the characteristic shape and size of this type of CNC, with a mean diameter 28 ± 13 nm and a length of 58 ± 15 nm.

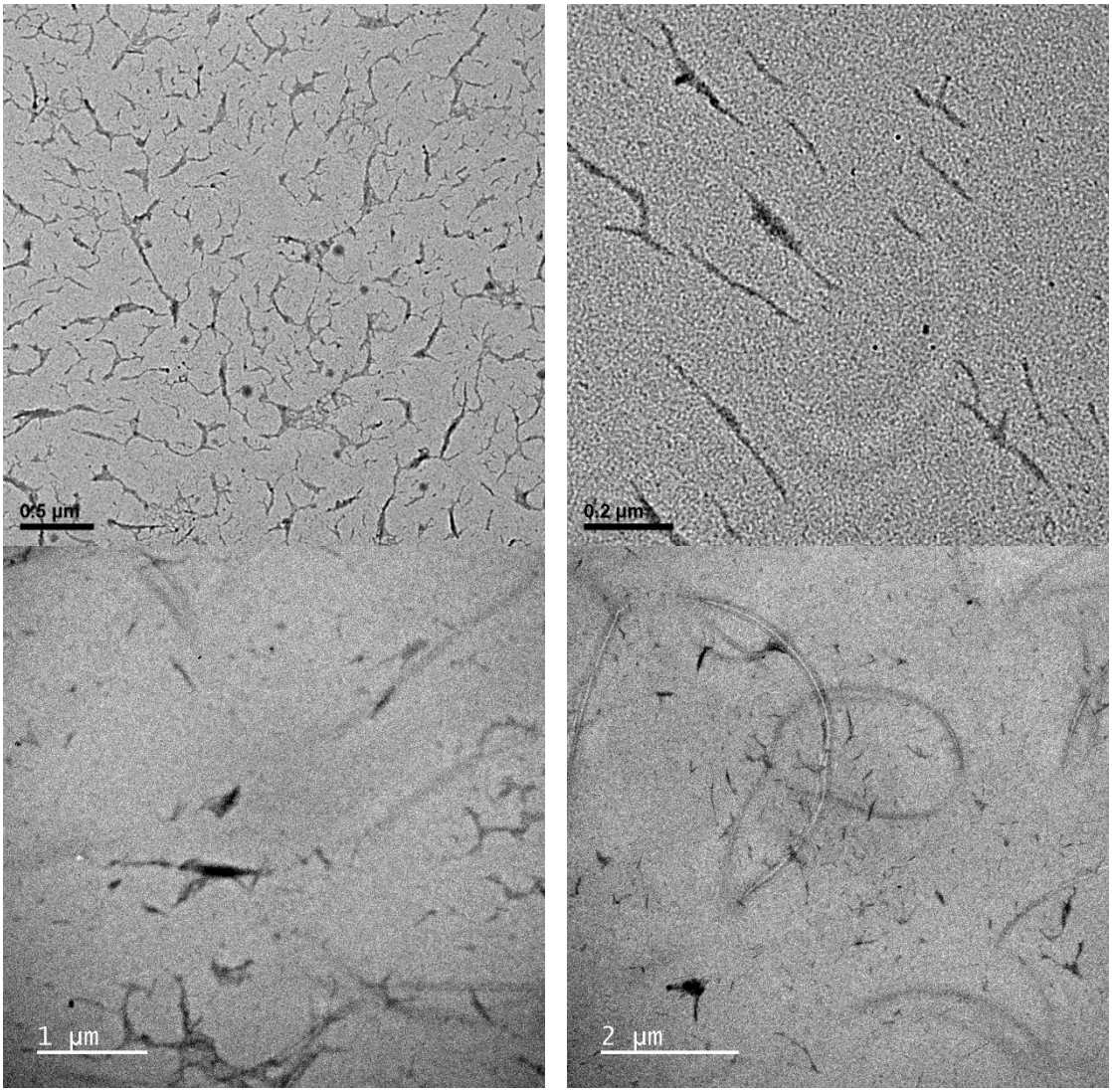

Figure S1: TEM images of type II CNCs. Reproduced with permission from reference [1]. Copyright © 2022, American Chemical Society.

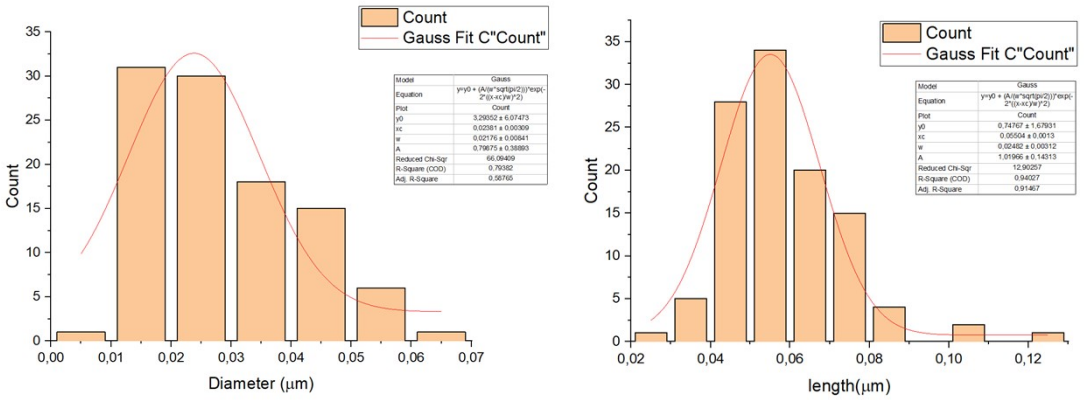

Figure S2: Statistical results of the diameter (left) and the length (right) of CNC II. Reproduced with permission from reference [1]. Copyright © 2022, American Chemical Society.

Type II CNCs were analyzed to determine their composition by elemental analysis and the results are presented in **Table S1**. The most characteristic result is the relative high mass percentage of sulfur of 3.45%, which is clearly higher than the value in type I CNCs prepared by the same approach.[2] The elemental composition (C, H, N and S) of the CNCs was determined using a LECO 628 elemental analyzer (Velp Scientifica). The elemental analysis was performed in triplicate to ensure reproducibility, and the average values were reported.

Table S1. Mass composition in percentage of type II CNCs determined by elemental analysis.

	C (%)	*H (%)*	*N (%)*	*S (%)*
Type II CNCs	36.9	5.88	0.24	3.45

Commercial TiO_2 paste (TiO_2-*P*): Film fabrication

The commercial paste (TiO_2-*P*) was dried in an oven at 120 ºC overnight to remove organic solvents and get a material ready for subsequent solid stated characterization such as XRD and TGA measurements.

For the preparation of the photoelectrodes using the commercial paste, an optimized screen-printing procedure was employed following the instructions provided by the supplier. The paste was applied to cover a 1 cm^2 surface area of the FTO substrates. Subsequently, the electrode was thermally sintered in an oven with the following temperature profile: 5 minutes at 325 ºC, 5 minutes at 375 ºC, 5 minutes at 450 ºC, and 15 minutes at 500 ºC, under an air atmosphere, according to the instructions from the provider. Prior to the photoelectrochemical (PEC) evaluation, the TiO_2 film was activated by treating it at 500 ºC in air for 30 minutes (**Figure S3**).

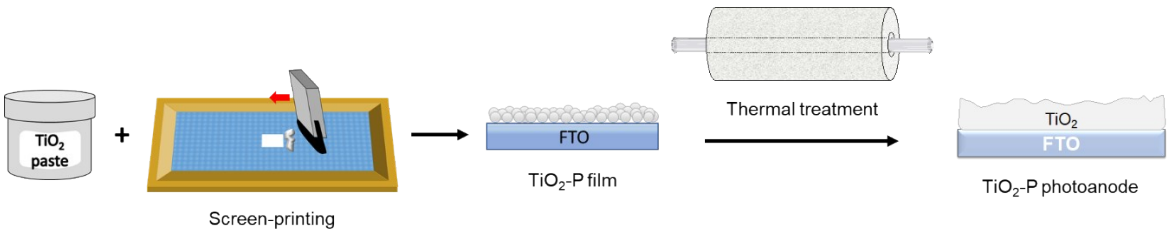

Figure S3. Preparation of screen-printed TiO_2 films on FTO substrates.

Preparation of $TiO_{2(NH4OH)}$ and solid material

$TiO_{2(NH4OH)}$ dispersions were prepared by mixing 50 mg of anatase powder, 300 µL of commercial aqueous ammonia (30%) and 19.7 mL of ultrapure water. Then, the resulting

mixture was homogenized in an ultrasonic bath for 1 h. Dispersions were freeze-dried to obtain powder materials for further characterization.

DLS and ζ-potential measurements

Typical DLS and ζ-potential measurements were shown in **Figure S4**. The specific values of $TiO_{2(NH4OH)}$ were depicted in **Table S2**.

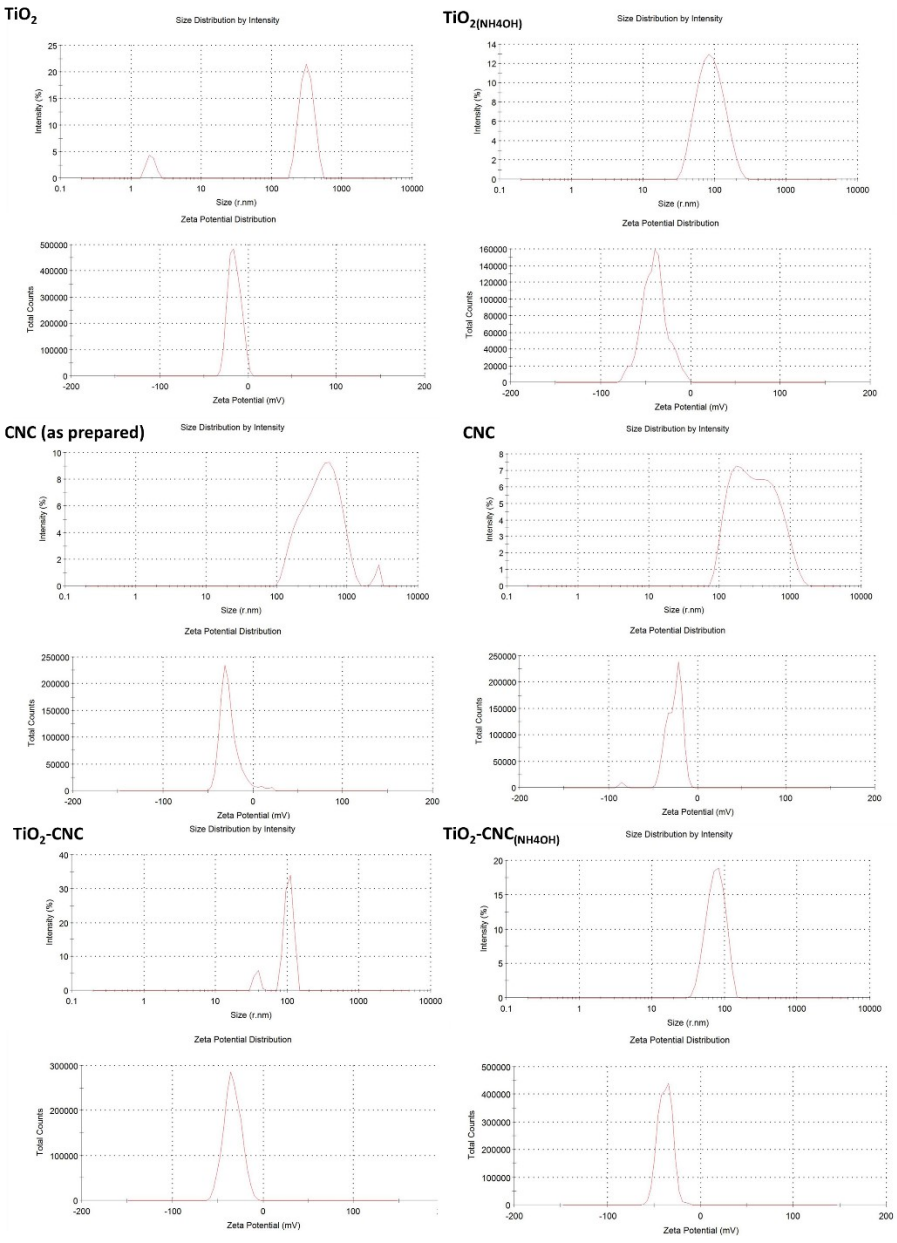

Figure S4. DLS and ζ-potential of the aqueous colloids.

Table S2. Hydrodynamic radius (R_H) from DLS and ζ-potential measurements of $TiO_{2(NH4OH)}$ dispersions (measurements were performed in triplicate).

	$TiO_{2(NH4OH)}$
R_H (nm)	95 ± 2
ξ-Potential (mV)	-37 ± 1

UV-Vis of the employed materials

Figure S5a shows the transmittance curves of various aqueous dispersions, including freshly prepared TiO_2-NPs, $TiO_{2(NH4OH)}$, CNC materials, and the $TiO_{2(NH4OH)}$ material after 24 hours of dispersion preparation. At the selected wavelength of 360 nm, the TiO_2-NPs dispersion exhibits the highest transmittance, indicating an unstable system with most of the material settling down. Conversely, the $TiO_{2(NH4OH)}$ material shows lower transmittance values, which moderately increases after 24 hours, evidencing successful dispersion of the TiO_2-NPs when ammonia was used. **Figure S5b** shows the variation of the transmittance for the $TiO_{2(NH4OH)}$, TiO_2-CNC and TiO_2-$CNC_{(NH4OH)}$ materials with time. The results demonstrate the effective role of ammonia in facilitating the dispersion of TiO_2-NPs, although CNC exhibited superior stabilization efficiency. Notably, the combination of ammonia and CNC yields the most stable aqueous dispersions, as evidenced by consistent transmittance values even after 24 hours.

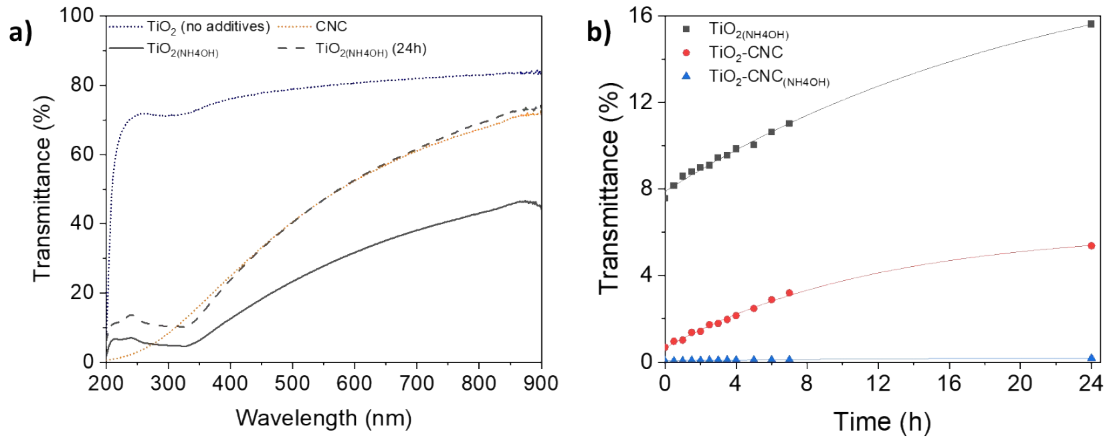

Figure S5. Transparency measurements of the waterborne TiO_2 dispersions. **a)** UV-vis transmittance of each TiO_2 dispersion both immediately after preparation and after settling for 24 h; and **b)** Transparency given in transmittance percentage at different times at a wavelength of 360 nm.

TEM of the $TiO_{2(NH4OH)}$ material

TEM images in **Figure S6** reveal the presence of TiO_2 aggregates, typically smaller than 100 nm. It seems that the addition of NH_4OH during the preparation of the TiO_2-NPs dispersion effectively disrupt the formation of large aggregates.

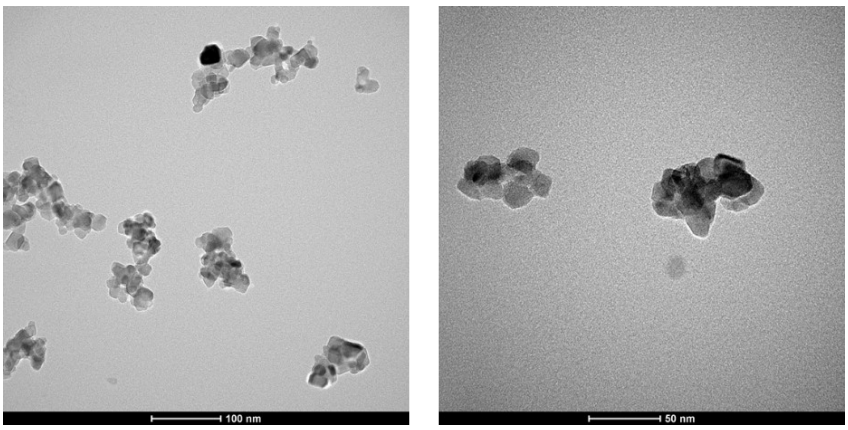

Figure S6. TEM images of the $TiO_{2(NH4OH)}$ dispersions.

Thermogravimetric analysis of CNC

All thermogravimetric analysis (TGA) of powder materials were carried out under air atmosphere in a Libra F1 (Netzsch) thermobalance using a ramp of 10 ºC/min. **Figure S7** confirms that CNC have been completely eliminated, as there is no residual mass after the experiment.

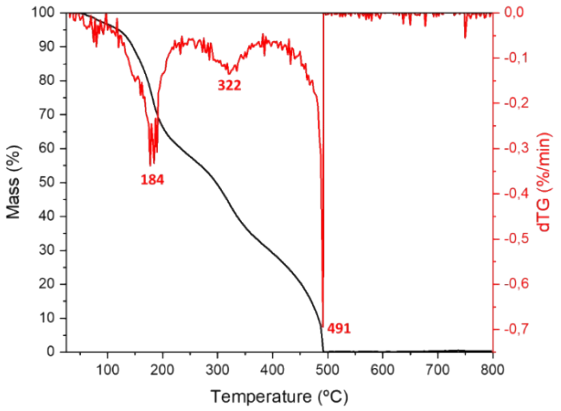

Figure S7. Thermogram of the employed CNC.

Thermogravimetric analysis of the TiO_2-CNC material

As the CNC residue is 0% at 800 ºC and approximately of 5% at 450 ºC, it can be deduced that CNC have been completely removed from the TiO_2 matrix during the sintering step (450 ºC, 2 hours). The TiO_2-CNC material reveals a 50% of residual mass, which confirms that all CNC were removed at a 1:1 TiO_2 : CNC ratio (**Figure S8**).

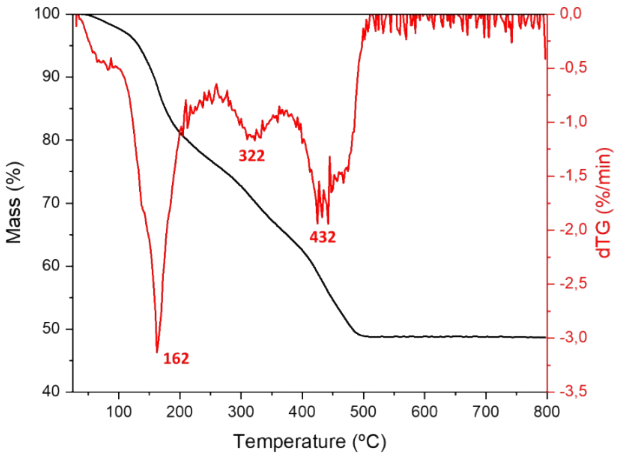

Figure S8. Thermogram of the resulting TiO_2-CNC hybrid for a given ratio of 1:1.

Differences in surface morphology between films prepared from commercial TiO_2-*P* and TiO_2-$CNC_{(NH4OH)}$

Figure S9 shows the results from the profilometry measurements of TiO_2-*P* and TiO_2-$CNC_{(NH4OH)}$ films. Both films displayed remarkable differences in surface characteristics**.** While TiO_2-*P* film shows a smooth surface, the film obtained from the TiO_2-$CNC_{(NH4OH)}$ dispersion exhibits a significant higher roughness. This disparity is clearly a consequence of the respective fabrication methodologies. In the case of the TiO_2-*P*, screen printing was employed, allowing the particles to accommodate under the gentle pressure of the printing blade, resulting in a roughness of 110 nm (**Figure S9a**). By contrast, the spray coating process immobilized the TiO_2-NPs upon contact with the hot substrate, leading to rapid droplet evaporation and the formation of a film with a pronounced roughness of 1300 nm **(Figure S9b**).

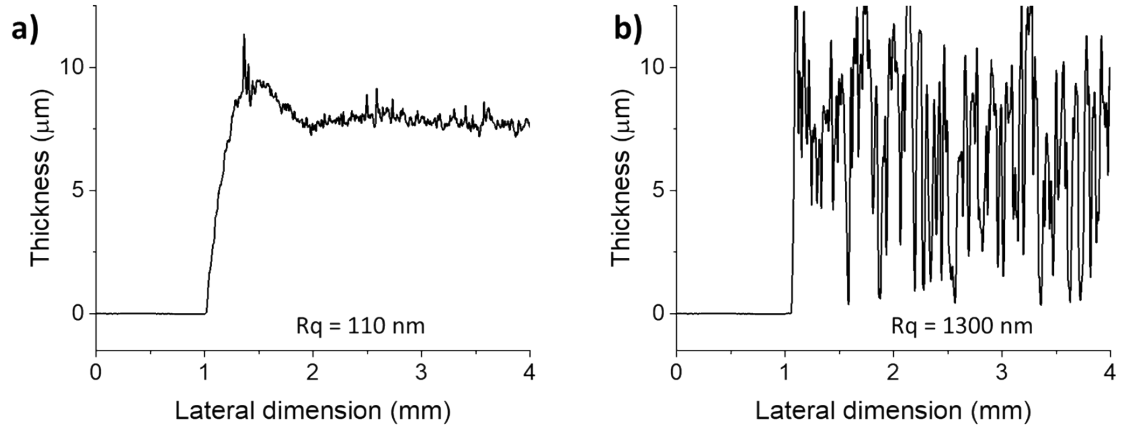

Figure S9. Profiles and quadratic roughness (Rq) of the TiO_2-based films fabricated by different methodologies: **a)** TiO_2-*P* profile and **b)** TiO_2-$CNC_{(NH4OH)}$ profile. Both films display an average thickness value of approximately 7 microns.

Effect of CNC in the surface morphology. Comparison between films prepared from commercial TiO_2-*P* and $TiO_{2(NH4OH)}$

To gain more insight into the effect of film processing, namely screen printing and spray coating, a comparison between TiO_2 photoanodes of the same thickness (~3.5 µm) prepared by both techniques is herein shown. The screen-printed TiO_2 photoanode was prepared with the GreatCell® paste, whereas the spray-coated TiO_2 photoanode was fabricated from the $TiO_{2(NH4OH)}$ dispersions in order to discard the CNC effect upon sintering, as described in the main article. In terms of surface morphology, it is of great interest the study of such property according to the followed fabrication procedure. As commented before, the screen-printed films display low Rq values (**Figure S10a**) whereas the $TiO_{2(NH4OH)}$ ones show a higher roughness (**Figure S10b**). These differences directly arise from the film fabrication method followed. Furthermore, the addition of CNC clearly influences the morphology of the film, with the bare $TiO_{2(NH4OH)}$ film

showing lower roughness (900 nm, **Figure S10b**) compared to the TiO_2-$CNC_{(NH4OH)}$ one (1300 nm, **Figure S9b**).

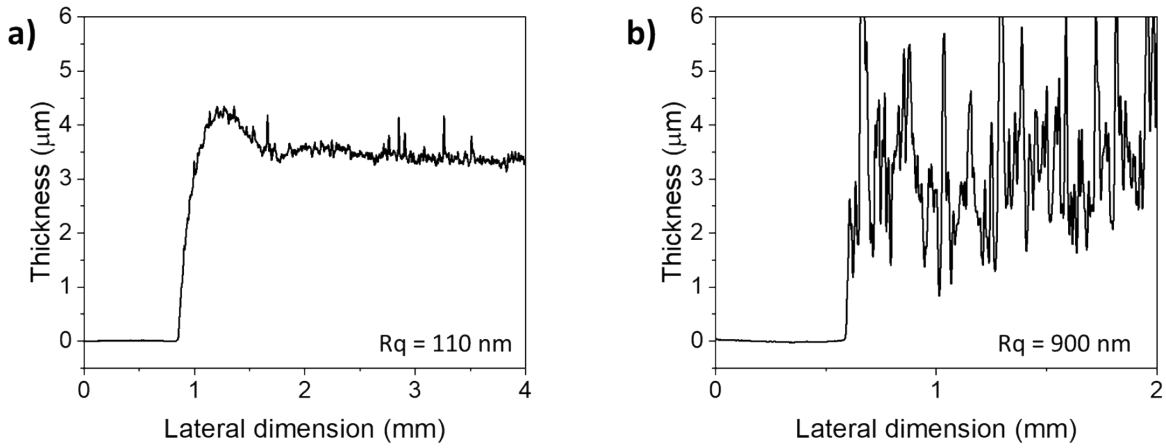

Figure S10. Profiles of the TiO_2 photoanodes prepared by **a)** screen printing and **b)** spray coating. Both films display a thickness of approximately 3.5 µm.

Gas physisorption of the TiO_2 materials (N_2 isotherms)

To further explore the effect of the CNC on the macroporous structure of the TiO_2-$CNC_{(NH4OH)}$ material used as photoanode, physisorption measurements were conducted on both bare TiO_2-NPs and TiO_2-$CNC_{(NH4OH)}$ powder materials after sintering. N_2 adsorption−desorption at -196 °C (Quantachrome Autosorb-6B Instrument) was measured after sample degassing (250 °C, 4 h) to characterize the porous texture and the equivalent Brunauer−Emmett−Teller (BET) specific surface area (S_{BET}). **Figure S11** shows the N_2 isotherms of the employed materials. Both materials exhibit type II isotherms according to the IUPAC classification, typical of non-porous solids.[1] The isotherms (**Figure S11**) reveal an initial increase at low relative pressure values. When it comes to the intermediate region of the isotherms, it is important to note that the TiO_2-

CNC hybrid has a slightly increased adsorption due to the removal of the biopolymer during the thermal treatment. This probably refers to an enlarged separation between the solid TiO_2 particles. A narrow hysteresis loop appears at very high relative pressures, around $p/p^0 = 0.9$, which is commonly ascribed to the capillary condensation taking place within the interstitial pores between TiO_2 particles.

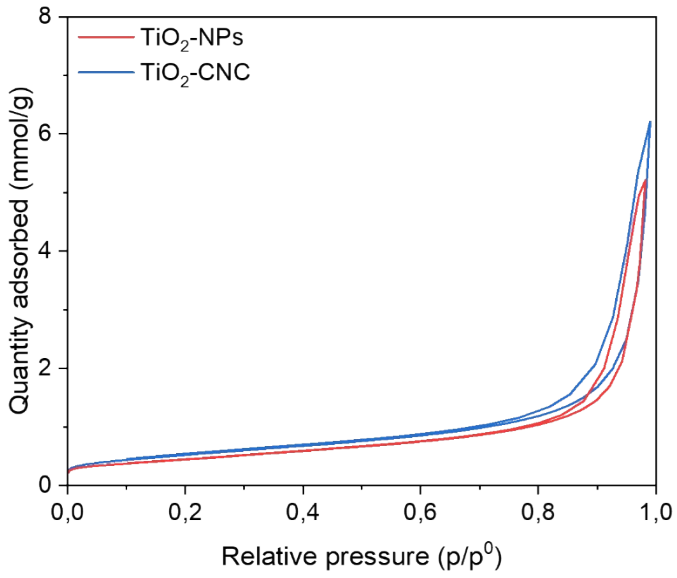

Figure S11. N_2 isotherms of the TiO_2 (anatase powder, red) and lyophilized TiO_2-CNC powder thermally treated at 450 ºC, 2h (blue).

The BET specific surface area of the TiO_2-$CNC_{(NH4OH)}$ powder material is marginally higher (42 m^2/g) to the observed for the bare TiO_2 nanoparticles (35 m^2/g), evidencing not too much influence of the CNC in the final internal porosity.

Pore size distribution (DFT and BJH methods)

Pore size distribution has been calculated for both samples from their N_2 adsorption isotherms using the density functional theory (DFT) (**Figure S12**) and the Barrett-Joyner-Halenda (BJH) method (**Figure S13**), which uses the Kelvin model of pore filling.

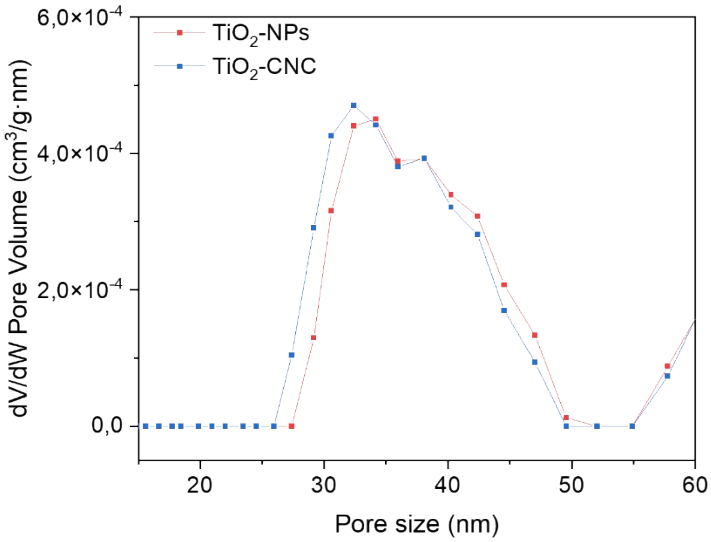

Figure S12. Pore size distribution obtained by the DFT method.

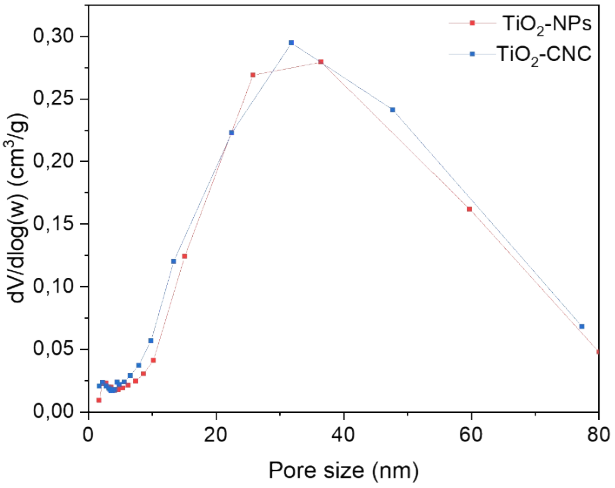

Figure S13. Pore size distribution calculated by the BJH method.

X-Ray diffraction

X-ray diffraction results of the employed materials, namely CNC (type-II), TiO_2-NPs (anatase), TiO_2-CNC, and the commercial TiO_2 paste (GreatCell®) are shown in **Figure S14**. The diffractogram of CNC (type-II) is in agreement with literature.[1,2] The

synthesized TiO_2-NPs exhibits the characteristic profile of anatase NPs, evidencing a comparable crystal phase composition and crystallite size to the commercial TiO_2 paste. The average crystallite size of the employed TiO_2-NPs is 25 nm,[3] whereas the commercial TiO_2 paste is composed of particles distributed in two sizes: 20 and 300 nm. Notably, the XRD analysis of the prepared TiO_2-$CNC_{(NH4OH)}$ hybrid shows a combined pattern from TiO_2 and CNC, not showing any additional peaks.

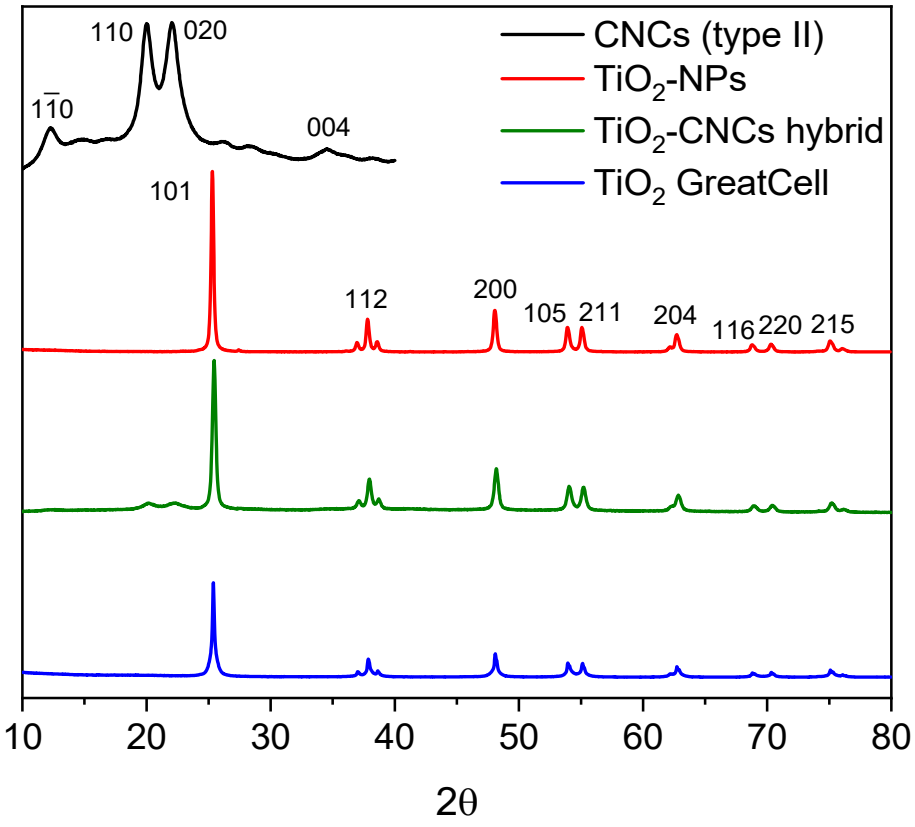

Figure S14. X-Ray diffractograms of the employed materials.

Thermogravimetric analysis of the commercial TiO_2 paste

The concentration of TiO_2 in the commercial paste is somewhat higher (62%, **Figure S15**) to that of the TiO_2-CNC. This mass loss is ascribed to the removal of alkylated celluloses from the paste.

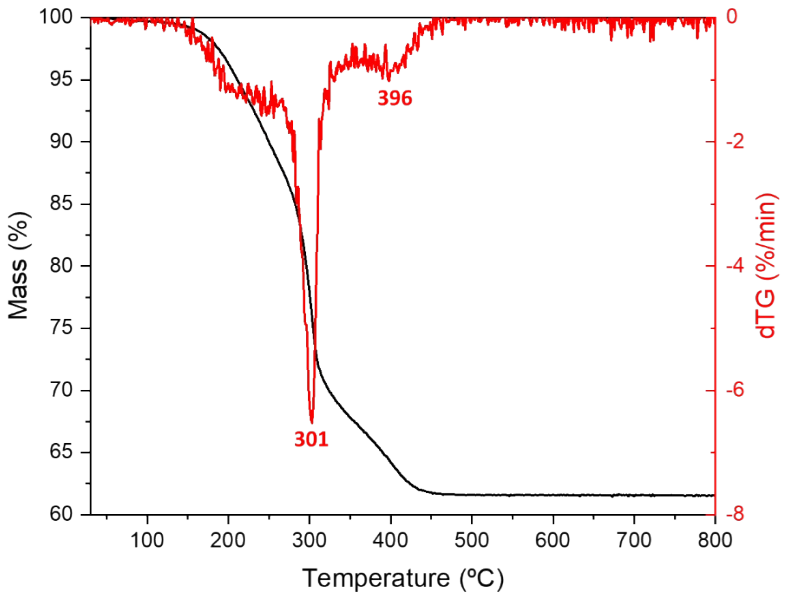

Figure S15. Thermogram of the commercial TiO_2 paste.

Scanning electron microscopy of photoanodes from commercial TiO_2-*P* based

Figure S16 shows SEM images of the film obtained from TiO_2 commercial paste. The TiO_2-*P* based photoelectrode film displays a smooth surface, both before and after air sintering, despite having a similar content of cellulose derivatives (62 wt.% of TiO_2) to our TiO_2-$CNC_{(NH4OH)}$ hybrid (50 wt.%) (**Figure S8**)

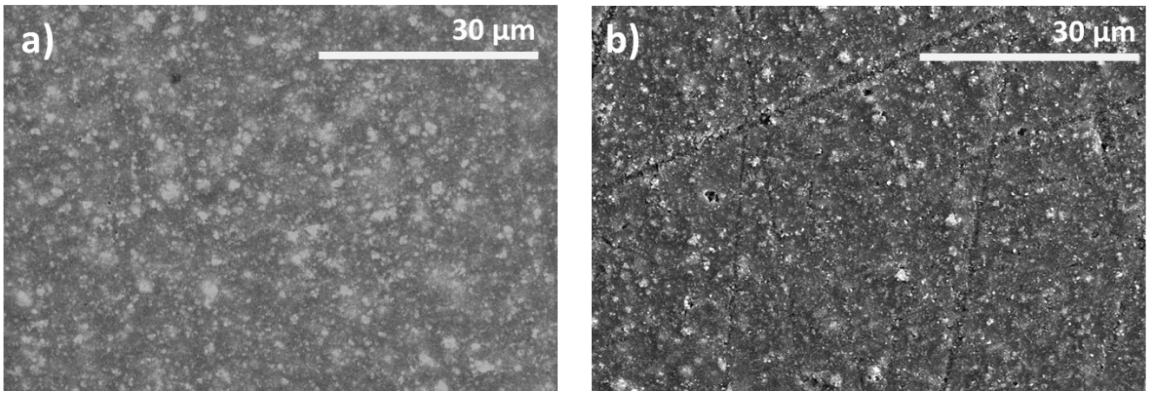

Figure S16. SEM images at different stages of the employed TiO_2 photoanodes. **a)** TiO_2-*P* electrode before sintering and **b)** TiO_2-*P* electrode after sintering.

Photoelectrochemical characterization of the films prepared from $TiO_{2(NH4OH)}$ and commercial TiO_2-*P*

Figure S17 displays the CV profiles of the $TiO_{2(NH4OH)}$ and TiO_2-*P* films, both under dark and illumination. In the absence of light, the photoelectrodes exhibit the characteristic reversible redox behavior of TiO_2 electrodes. A cathodic current is observed at more negative potentials, and a nearly symmetric positive current during the backward scan. The voltammograms exhibited an accumulation region at approximately -0.8 V, and a depletion region at higher potentials, -0.4 V. Under illumination conditions, both materials show similar photocurrent values (~ 46 $\mu A \cdot cm^2$).

This observation is further supported by transient photocurrent measurements (**Figure S18)**, which reveal slight differences between the two electrodes (from 32 $\mu A \cdot cm^{-2}$ to 43 $\mu A \cdot cm^{-2}$), highlighting the significant improvement of the TiO_2 electrodes when using CNC and ammonia for their fabrication.

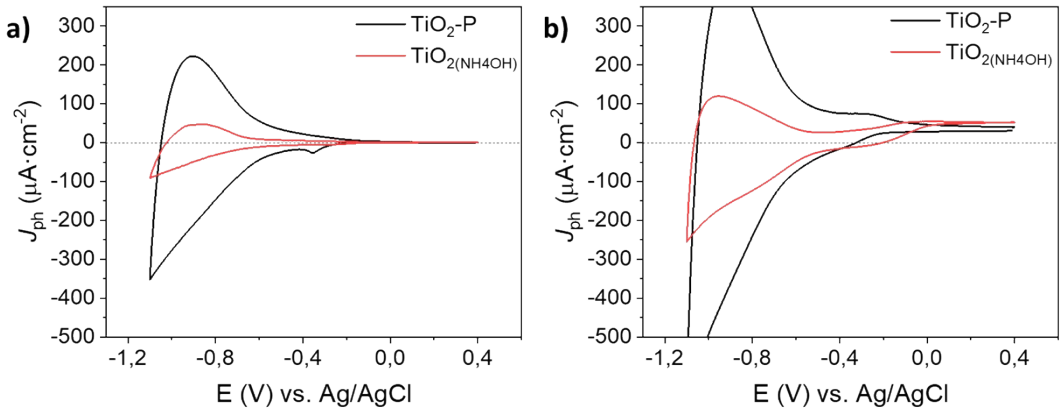

Figure S17. CV of the TiO_2 photoanodes under **a)** dark and **b)** light irradiation conditions.

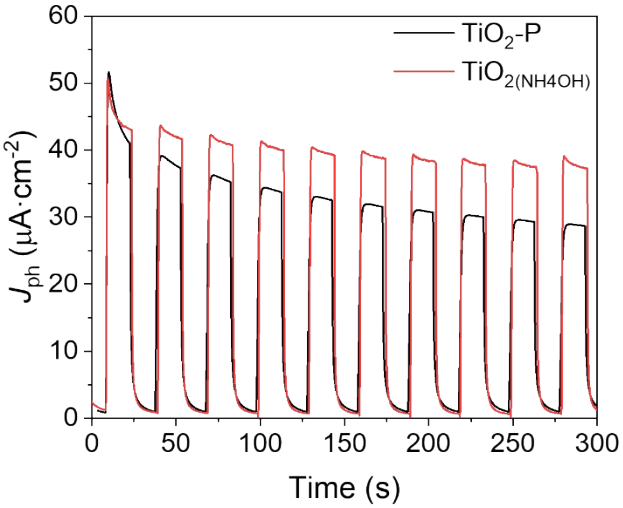

Figure S18. Transient photocurrent measurements of the screen-printed TiO_2-*P* photoanodes (**black**) and spray-coated $TiO_{2(NH4OH)}$ photoanodes (**red**).

5-hour photocurrent measurements

Aiming to study the stability of the TiO_2-$CNC_{(NH4OH)}$ and TiO_2-*P* photoanodes, 5-hour experiments at a constant potential (0 V vs. Ag/AgCl) were performed (**Figure S19**). A photocurrent decay is observed in both cases, mainly caused by the blocking of the TiO_2 active sites due to parasitic redox processes (see references 33, 34 and 35). Nevertheless, the TiO_2-$CNC_{(NH4OH)}$ retained a higher PEC performance, even after 5 hours under operation conditions due to its specific morphology that arises from the CNC processing.

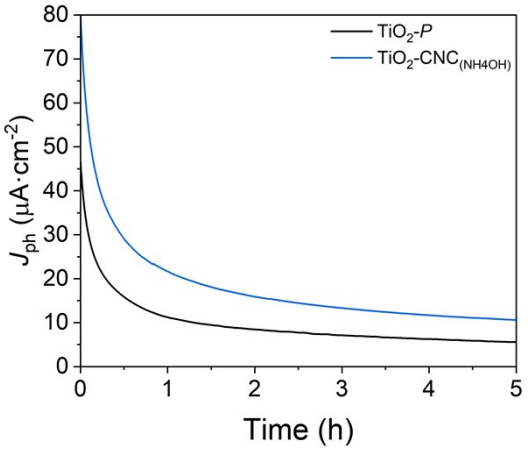

Figure S19. 5-hour photocurrent experiments measured at 0 V (vs. Ag/AgCl).

Electrochemical impedance spectroscopy (EIS). Equivalent circuit

EIS spectra were analyzed according to the model circuit shown in **Figure S20**.[4] Resistances (R_S, R_{ct} and R_{sc}) and constant phase elements, i.e. non-ideal capacitors with phase angle <90, (CPE_{dl} and CPE_{sc}) are calculated as model fitting parameters to the experimental data.

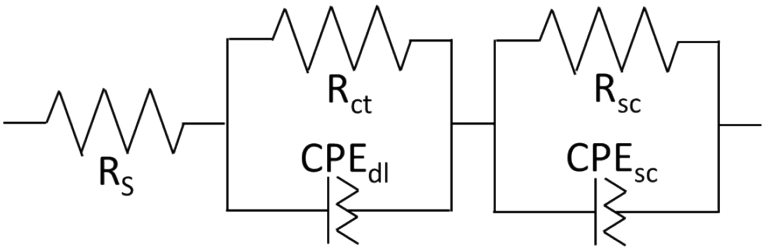

Figure S20. Equivalent circuit used to fit EIS measurements.

C_{dl} and C_{sc} were obtained from the **Equation S1**:

$$Z_{CPE} = \frac{1}{j\omega C^{\alpha}} \qquad \textbf{(Equation S1)}$$

where Z_{CPE} is the impedance of the constant phase element, α an empirical constant comprised between 0 and 1,[4] and C the calculated capacitance.

Particularly, S refers to the electrolyte solution and to the substrate, subscript dl double layer) is associated to the TiO_2 film/electrolyte interface, and subscript sc (space charge) is associated to the TiO_2 film/FTO interface impedance.

References

(1) Calvo, V.; Álvarez Sánchez, M. Á.; Güemes, L.; Martínez-Barón, C.; Baúlde, S.; Criado, A.; González-Domínguez, J. M.; Maser, W. K.; Benito, A. M. Preparation of Cellulose Nanocrystals: Controlling the Crystalline Type by One-Pot Acid Hydrolysis. *ACS Macro Letters* **2023**, *12*, 152–158. https://doi.org/10.1021/acsmacrolett.2c00705.

(2) González-Domínguez, J. M.; Ansón-Casaos, A.; Grasa, L.; Abenia, L.; Salvador, A.; Colom, E.; Mesonero, J. E.; García-Bordejé, J. E.; Benito, A. M.; Maser, W. K. Unique Properties and Behavior of Nonmercerized Type-II Cellulose Nanocrystals as Carbon Nanotube Biocompatible Dispersants. *Biomacromolecules* **2019**, *20* (8), 3147–3160. https://doi.org/10.1021/acs.biomac.9b00722.

(3) Cano-Casanova, L.; Ansón-Casaos, A.; Hernández-Ferrer, J.; Benito, A. M.; Maser, W. K.; Garro, N.; Lillo-Ródenas, M. A.; Román-Martínez, M. C. Surface-Enriched Boron-Doped TiO_2 Nanoparticles as Photocatalysts for Propene Oxidation. *ACS Applied Nano Materials* **2022**, 5, 12527-12539. https://doi.org/10.1021/acsanm.2c02217.

(4) Lopes, T.; Andrade, L.; Le Formal, F.; Gratzel, M.; Sivula, K.; Mendes, A. Hematite Photoelectrodes for Water Splitting: Evaluation of the Role of Film Thickness by Impedance Spectroscopy. *Physical Chemistry Chemical Physics* **2014**, *16* (31), 16515–16523. https://doi.org/10.1039/c3cp55473b.